Efficient and scalable atmospheric water harvesting in arid climate enabled by thin polyampholyte hydrogel layer

Supplementary Information Table of Contents

Supplementary Notes

Supplementary Figures

Supplementary Notes

Supplementary Note 1: Sorption kinetics of P(AA_x-*co*-$AETAC_y$) loaded with LiCl

The water vapor sorption curves indicated that when LiCl content was 50 wt% (Supplementary Fig. 3a), P(AA_1-*co*-$AETAC_3$) and P(AA_0-*co*-$AETAC_1$) showed closed sorption kinetics. However, when LiCl content reached 60 and 70 wt%, P(AA_1-*co*-$AETAC_3$) was first to reach equilibrium (Supplementary Fig. 3b and 3c). These could be attributed to the strong interaction between the ionic group of P(AA_1-*co*-$AETAC_3$) and LiCl. When LiCl content was low (50 wt%), P(AA_x-*co*-$AETAC_y$) samples showed enough interaction with LiCl to prevent agglomeration. However, when LiCl content increased (larger than 60 wt%), more LiCl may have agglomerated in other samples compared with P(AA_1-*co*-$AETAC_3$), thus slowing the sorption kinetics.

Supplementary Note 2: AWH performance of HPHMs

The water vapor capacity and sorption rate of HPHMs was significantly affected by the mass fraction between P(AA_1-*co*-$AETAC_3$) and LiCl aqueous solution. For P(AA_1-*co*-$AETAC_3$) immersed in 4.2 wt% LiCl (Supplementary Fig. 6a and 6b), 8.4 wt% LiCl (Supplementary Fig. 6c and 6d), and 12.6 wt% LiCl (Supplementary Fig. 6e and 6f) aqueous solution, the water vapor capacities and sorption rate were all increased with the increasing of the mass fraction of LiCl aqueous solution in the mixed solution of P(AA_1-*co*-$AETAC_3$) and LiCl aqueous solution. The increase in water vapor capacity was attributed to more LiCl being loaded in P(AA_1-*co*-$AETAC_3$). The mass of HPHMs adhered to nylon mesh per square meter decreased with the decrease of P(AA_1-*co*-$AETAC_3$) content in LiCl aqueous solution, which enlarged the water vapor-sorbent contact area and thus accelerated the sorption rate. In order to reduce experimental error, the mass fraction of LiCl aqueous solution was no longer increased when the mass of HPHMs adhered to the nylon mesh was less than 50 mg (The dimension of the test nylon mesh is 6.5 cm × 6.5 cm). Thus, we did not further decrease the mass fraction of P(AA_1-*co*-$AETAC_3$) in 4.2 wt% LiCl aqueous solution. The mass fraction of P(AA_1-*co*-$AETAC_3$) in 8.4 wt% and 12.6 wt% LiCl aqueous solution did not continue to decrease because this would cause HPHMs cannot adhere effectively to the nylon mesh. As a result, P(AA_1-*co*-$AETAC_3$) : 4.2 wt% LiCl = 1 : 30; P(AA_1-*co*-$AETAC_3$) : 8.4 wt% LiCl = 1 : 50; P(AA_1-*co*-$AETAC_3$) : 12.6 wt% LiCl = 1 : 50 (labeled as HPHMs-1, HPHMs-2, and HPHMs-3), respectively, were chosen as ideal candidates for further study.

Supplementary Note 3: Evaporation and melting behaviors of HPHMs with different LiCl content

Differential scanning calorimetry (DSC) was applied to measure the evaporation and melting behavior. The evaporation peak of HPHMs loaded with 10, 20, 40, 60, and 80 wt% LiCl content was 95, 95, 104, 110, and 128 ℃, respectively (water content was fixed at 2 g g^{-1}, Supplementary Fig. 9a). These results indicated that higher desorption temperature was needed to evaporate large portion of water with increasing of LiCl content. In addition, the melting point of HPHMs with 10, 20, and 40 wt% LiCl was -8, -15, and -30 ℃, respectively, and which from 60 and 80 wt% LiCl loading samples totally disappeared (Supplementary Fig. 9b). These results suggested that the amount of freezable water in HPHMs decreased with the increase of LiCl

content, and it disappeared when LiCl content was more than 60%. It should be noted that more energy was needed for desorption with the decrease of the freezable water amount[32].

Supplementary Note 4: Fabrication of water collection test device

In the design of the test device (Supplementary Fig. 14), positive temperature coefficient (PTC) heaters, which are embedded in an aluminum inner plate, are used to elevate the ambient temperature of the heating chamber to release the captured water. The air inlet and outlet enable the humid air being released from sorbents to circulate within the device through the vacuum pump, condense into liquid water in the polymer tube, and finally flow into the collecting glass bottle (Supplementary Video 5). Nylon mesh with HPHMs-1 was secured to a phenol formaldehyde plastic rack (80 mm×70 mm), and 24 racks were placed in vertical arrays with an interval of 2 mm to enable air flow freely.

Supplementary Note 5: Fabrication and performance of HPHMs-based automated SAWH system

The process of automatic water collection in a cycle can be divided into the following steps (Fig. 6b):

Step 1: Sorption. One sorption bed module is exposed to the air for water sorption. And cooling fans operate to increase airflow velocity, thereby accelerating the water sorption process.

Step 2: Desorption. After complete sorption, the sorption bed module sequentially performs descending, rotating, and ascending movements via the transmission module. Then, the sorption bed enters the heating module. An airtight heating chamber is built by the bottom insulation plate of the sorption bed and the heating module. The HPHMs adhered to the sorption bed module release water vapor upon high-temperature heating via heating elements.

Step 3: Collection. The water vapor is drawn from the heating module into the condenser, driven by the vacuum pump. It rapidly cools within the condenser, which is a spiral aluminum tube. Then the forming water stream flows into the water collector. Moreover, the outlet of the water collector is connected to the inlet of the pump, and the outlet of the pump is connected to the heating chamber to return the not fully condensed water vapor for condensing during the next cycle.

Step 4: Prepare for sorption. After completing the desorption and collection, the sorption bed within the heating module sequentially performs descent, rotation, and ascent movements via the transmission module (Supplementary Video 6). Then, the sorption bed enters the water sorption area. Simultaneously, another sorption bed with completed water sorption enters the heating module for desorption.

The 3D sorption bed module consists of nylon meshes, net frames, silicone rings, HPHMs, and a bottom insulation plate. There are 49 nylon meshes in each sorption bed module, which are arranged at specific intervals via net frames and silicone rings. The dimension of each nylon mesh is 120 mm × 120 mm, and each sorption bed module could load approximately 55 g HPHMs. The heating module is composed of aluminum alloy heat spreaders, heating elements, ultra-low thermal conductivity shells, and a silicone rubber seal (shown in Supplementary Fig. 17). There are air channels in two aluminum alloy heat spreaders that are perpendicular to the internal of nylon meshes during desorption. Numerous 1mm air holes are evenly distributed throughout the interior of the heating chamber. Thus, the desorption water vapor can be pumped to the condenser, and the not fully condensed water vapor can be returned to the heating

chamber. When the sorption module enters the heating modules, the dimensions of the heating chamber are 130 mm × 130 mm × 144 mm. The maximum heating power is approximately 550 W, powered by 60 V DC, and the temperature maintenance power is approximately 80 W, powered by 24 V DC. The temperature of heating elements was maintained at 165 ± 1 ℃ to provide sufficient heat flow while avoiding damage to nylon mesh, which is controlled by a PID controller.

Two sorption bed modules are up on a turnplate that is a part of the transmission module. When one performs the sorption, another enters the heating module to execute the desorption. The vacuum pump and cooling fans would work during the collection. The pump has a flow rate of 45 L min^{-1}, a maximum negative pressure of -85 kPa, and a power of 42 W, respectively. The total power of the fans is 24 W. The electrical control module, powered by 220 V AC, is composed of a PLC, temperature and humidity sensors, and power converters. Otherwise, a solar power module can also be used for energy supply when the device operates outdoors.

The dimensions of the automated SAWH device are 610 mm × 490 mm× 780 mm.

Supplementary Fig. 18 indicates that the water collection of HPHMs increased from 12.08 to 32.56 mL as the desorption time increased from 15 to 35 min. Meanwhile, the water collection rate increased from 0.80 to 0.94 mL min^{-1}. The maximum water collection rate was 0.97 mL min^{-1} when the desorption time was 30 min. Hence, sorption and desorption were all set to 30 min.

Supplementary Fig. 19 shows the photograph of the experimental setup, where the power and energy are calculated by a power meter, the data of temperature and humidity are acquired by a temperature and humidity sensor, and the mass change of the collected water is recorded by an electronic balance connected to a laptop.

Supplementary Figures

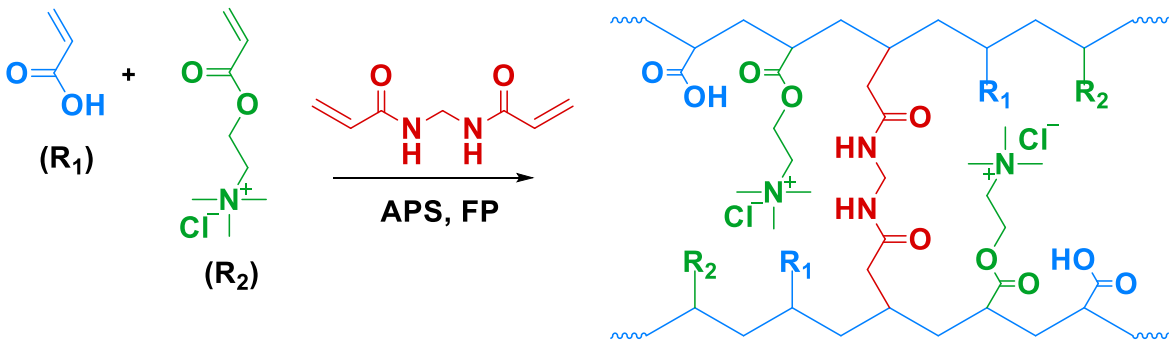

Figure S1. Synthesis of P(AA_x-*co*-$AETAC_y$).

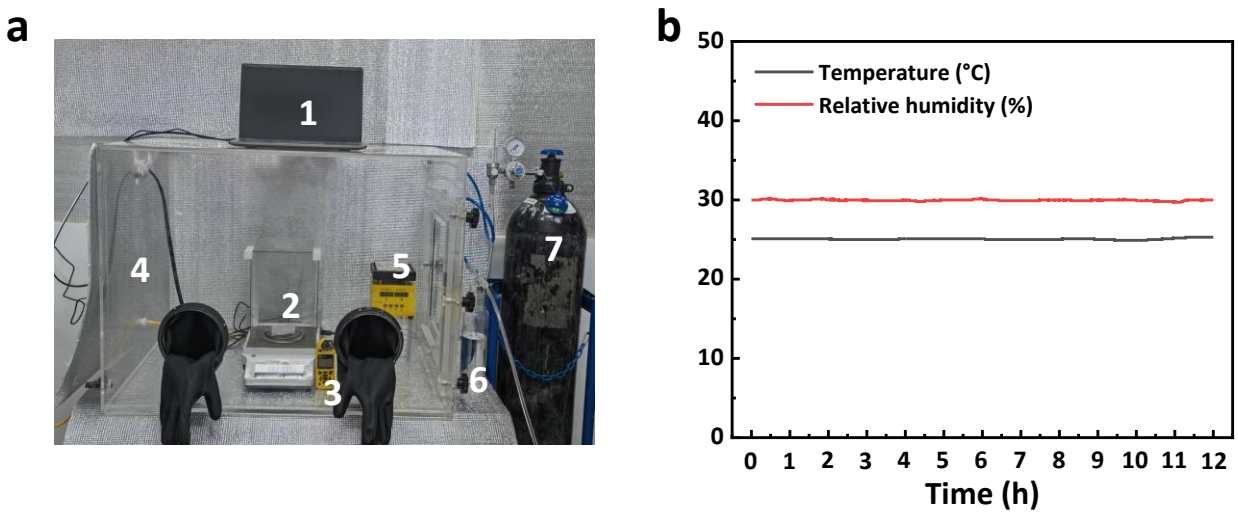

206

207 **Figure S2. Homemade vapor sorption test system setup.** (**a**) Homemade vapor sorption-
208 desorption test system. 1. laptop, 2. analytical balance, 3. weather meter, 4. acrylic chamber, 5.
209 heat plate, 6. gas-washing bottle, and 7. nitrogen cylinder (more details see methods). The
210 environmental temperature is controlled by the air conditioning system. (**b**) Temperature and
211 relative humidity of the test system.

212

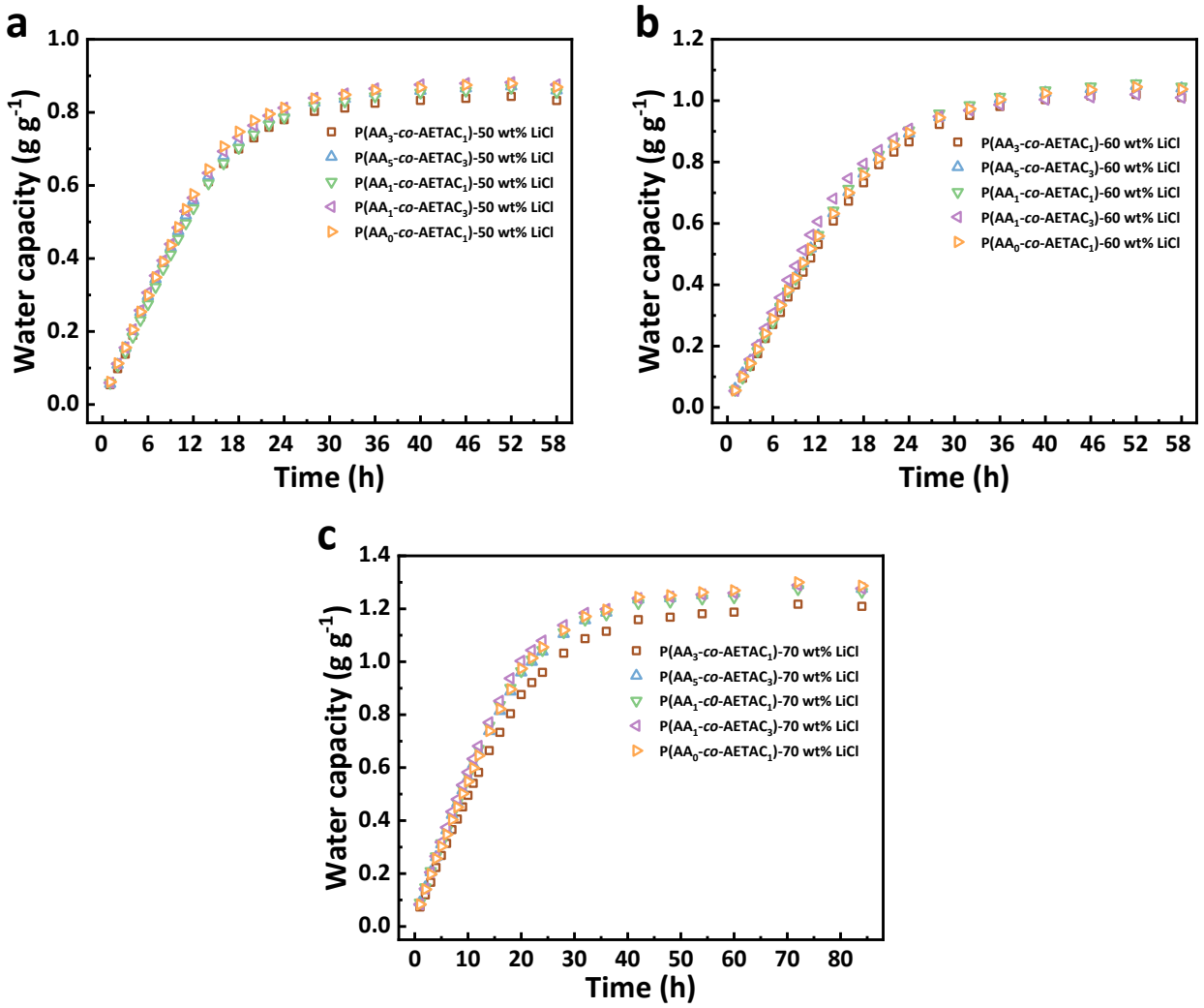

213

214 **Figure S3. Sorption kinetics of P(AA$_x$-*co*-AETAC$_y$) loaded with LiCl.** P(AA$_x$-*co*-AETAC$_y$)
215 loaded with (**a**) 50 wt% LiCl; (**b**) 60 wt% LiCl; (**c**) 70 wt% LiCl. The test condition was 25 °C,
216 30% RH.

217

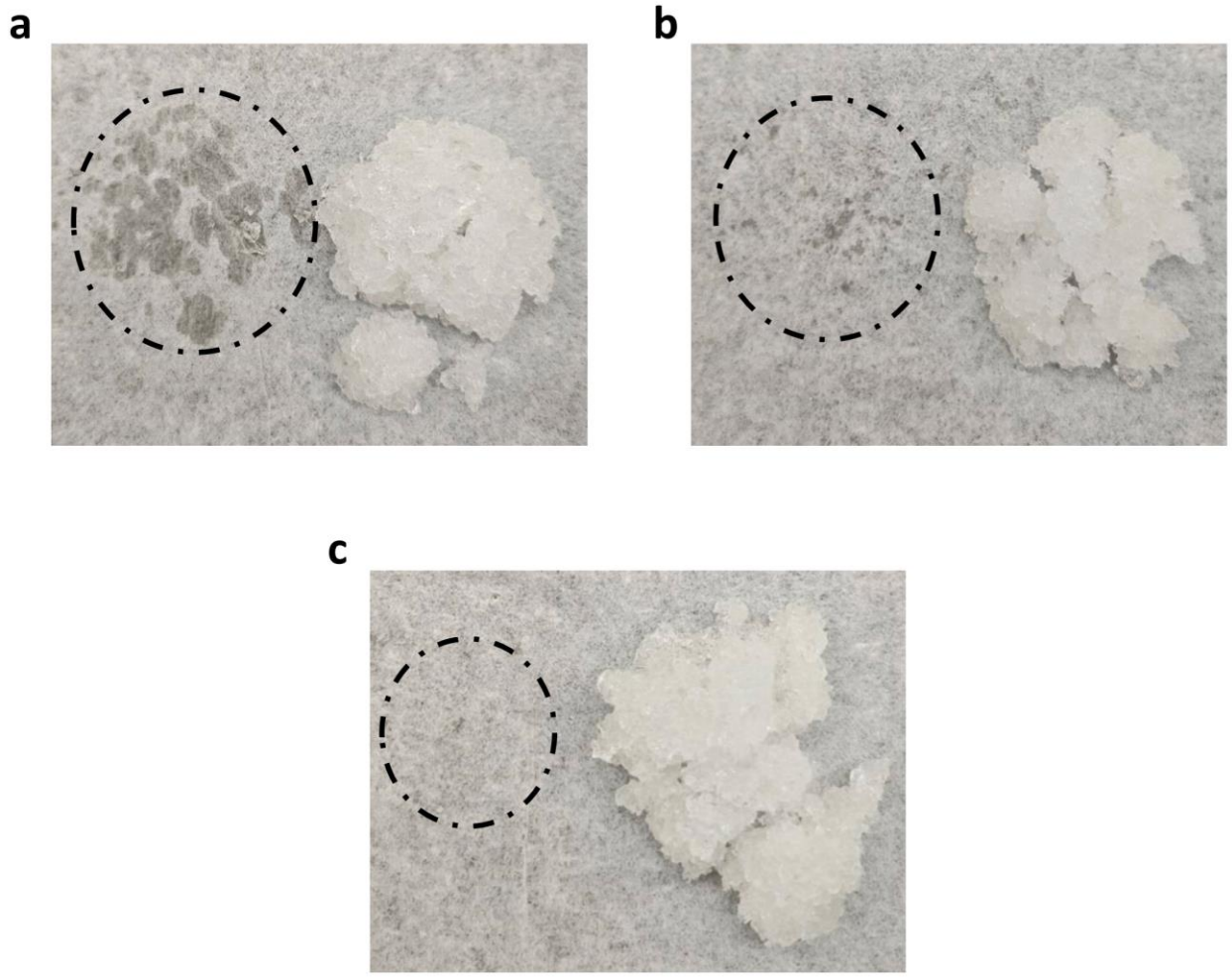

218

219 **Figure S4. Leakage measurement of P(AA$_1$-*co*-AETAC$_3$).** Photos of P(AA$_1$-*co*-AETAC$_3$)
220 loaded with LiCl after 48 h sorption under 25 ℃, 70% RH. (**a**) P(AA$_1$-*co*-AETAC$_3$): LiCl = 2: 8
221 (g g^{-1}); (**b**) 1.5: 7.5 (g g^{-1}); (**c**) 3: 7 (g g^{-1}).

222

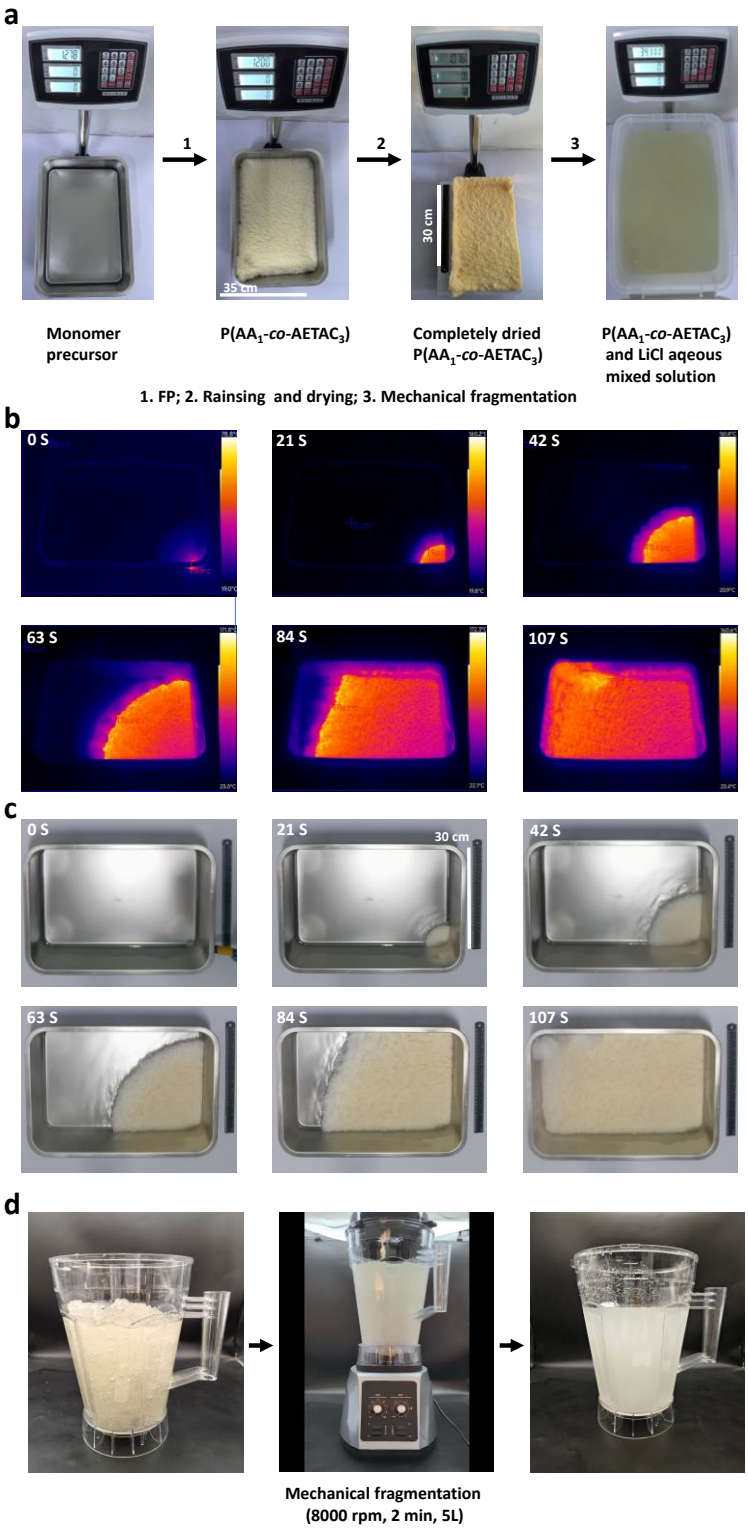

223 **Figure S5. Kg scale fabrication of HPHMs.** (**a**) The overall fabricating procedure of P(AA_1-*co*-
224 $AETAC_3$) and its LiCl aqueous mixed solution. FP of the (**b**) thermal infrared images and (**c**)
225 photos of 1 kg P(AA_1-*co*-$AETAC_3$). (**d**) Mechanical fragmentation of P(AA_1-*co*-$AETAC_3$) and
226 LiCl aqueous mixed solution.

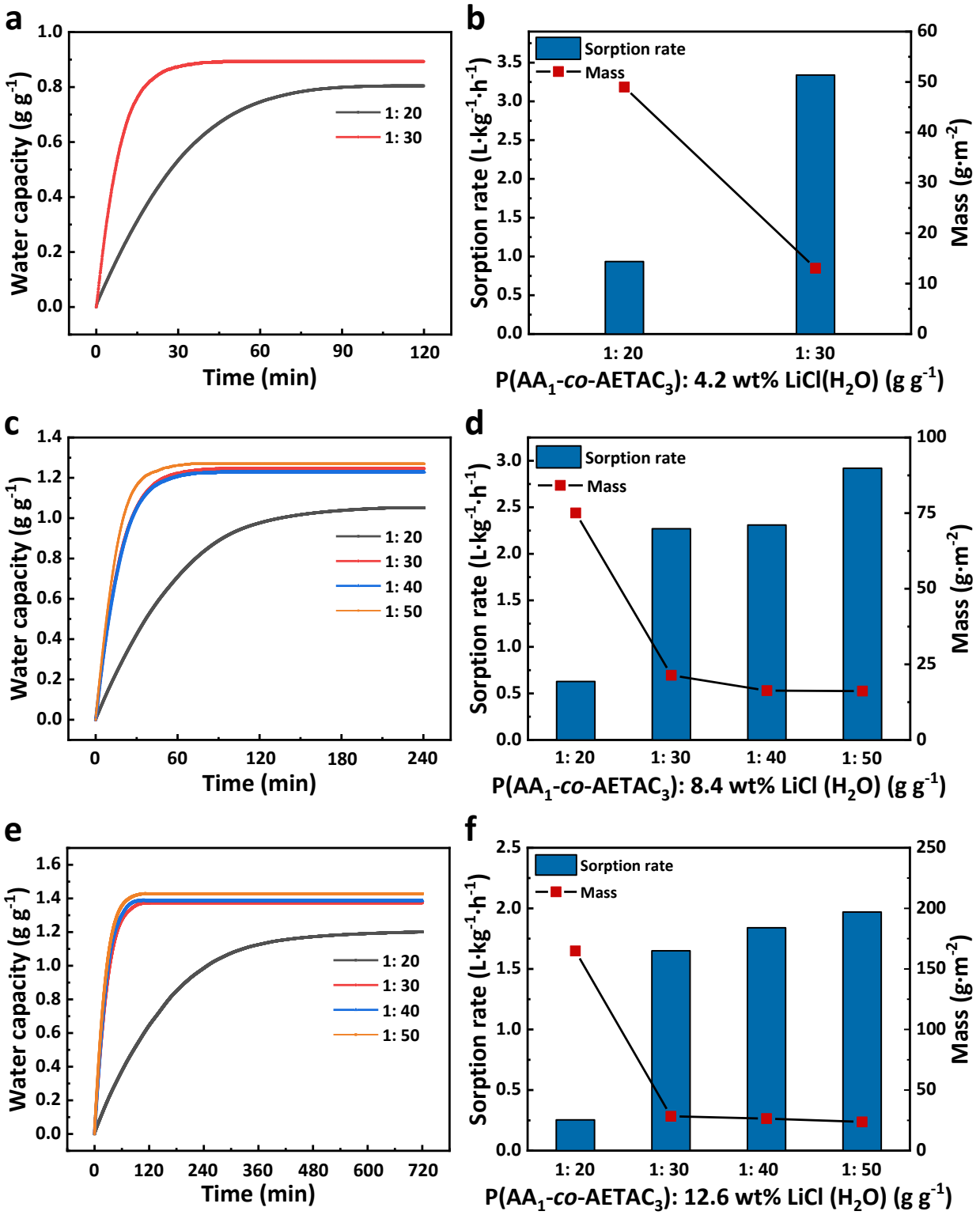

Figure S6. AWH performance of HPHMs. Water uptake, sorption rate, and mass of P(AA_1-*co*-$AETAC_3$) adhered to nylon mesh with different mass fractions and concentrations of LiCl aqueous solution. (**a, b**) P(AA_1-*co*-$AETAC_3$): 4.2 wt% LiCl = 1: 20, 1: 30 (g g^{-1}); (**c, d**) P(AA_1-*co*-$AETAC_3$): 8.4 wt% LiCl = 1: 20, 1: 30, 1: 40, and 1: 50 (g g^{-1}); (**e, f**) P(AA_1-*co*-$AETAC_3$): 12.6 wt% LiCl = 1: 20, 1: 30, 1: 40, and 1: 50 (g g^{-1}).

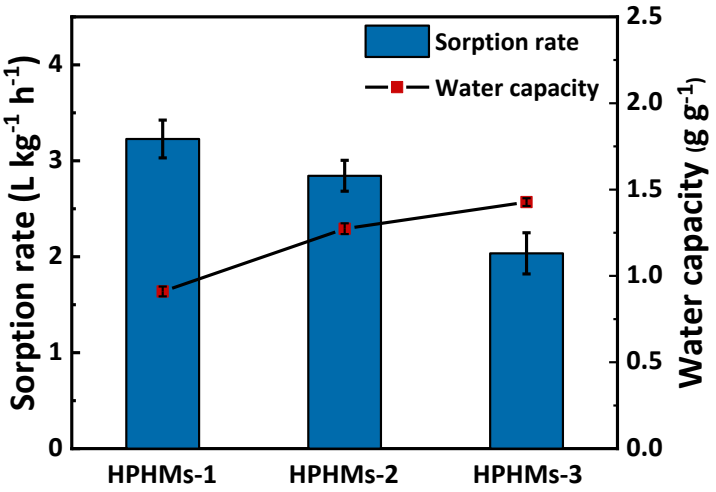

Figure S7. AWH performance of HPHMs-1, HPHMs-2, and HPHMs-3. Water uptake and sorption rate of P(AA_1-*co*-$AETAC_3$) with different mass fractions and concentrations of LiCl aqueous solution.

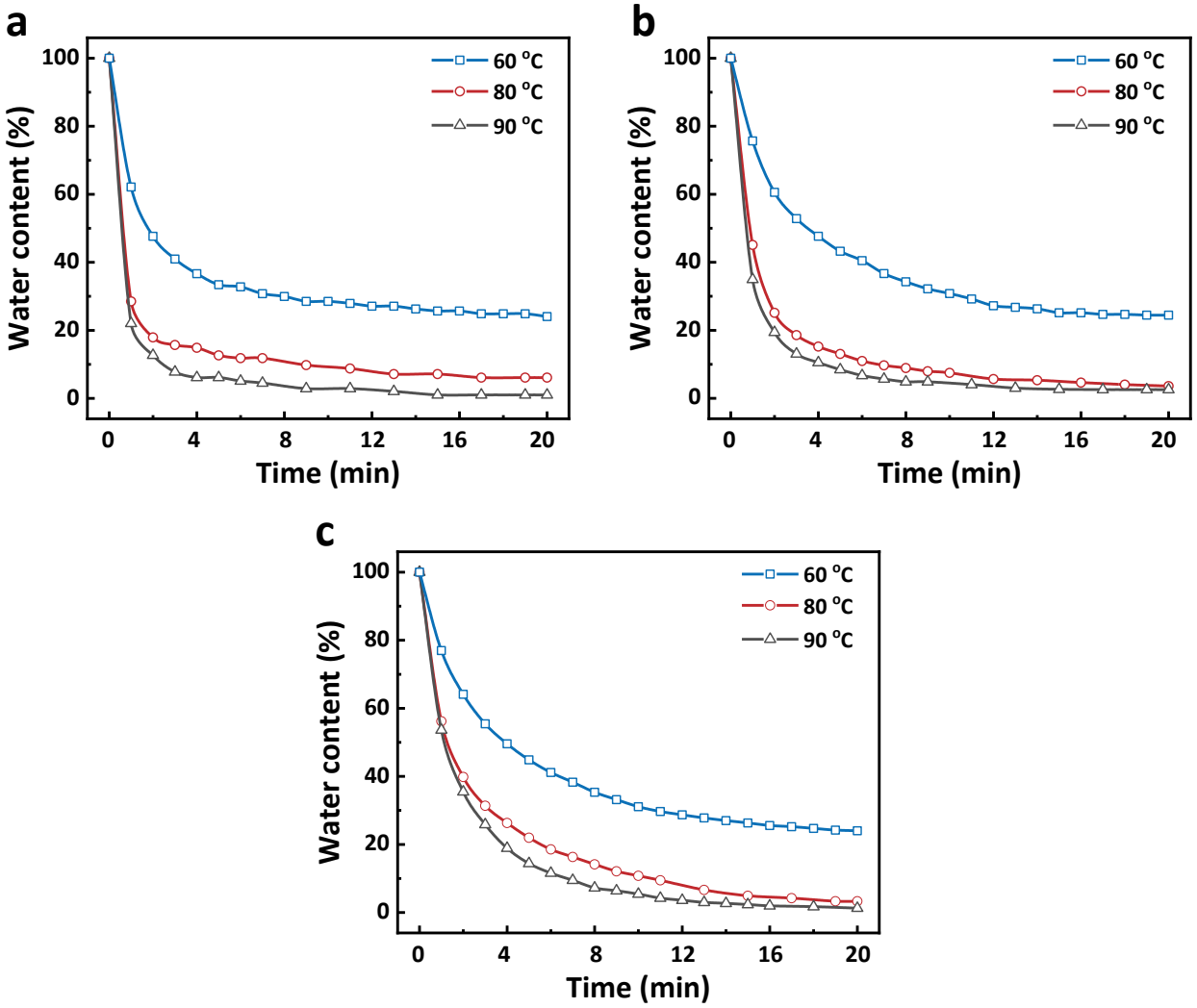

Figure S8. Desorption behavior of HPHMs-1, HPHMs-2, and HPHMs-3. Desorption curves of HPHMs under different desorption temperatures. (**a**) HPHMs-1; (**b**) HPHMs-2; (**c**) HPHMs-3.

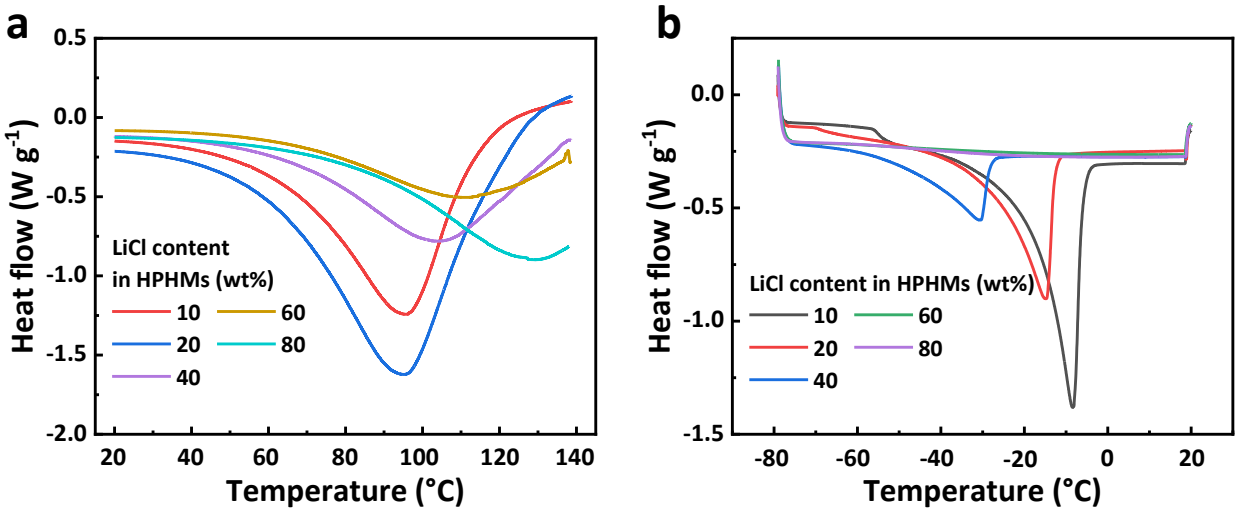

Figure S9. Evaporation and melting behavior of HPHMs with different LiCl content. Heat flow curves showing (**a**) evaporation and (**b**) melting behavior of HPHMs at the same water content of 2 g g^{-1}.

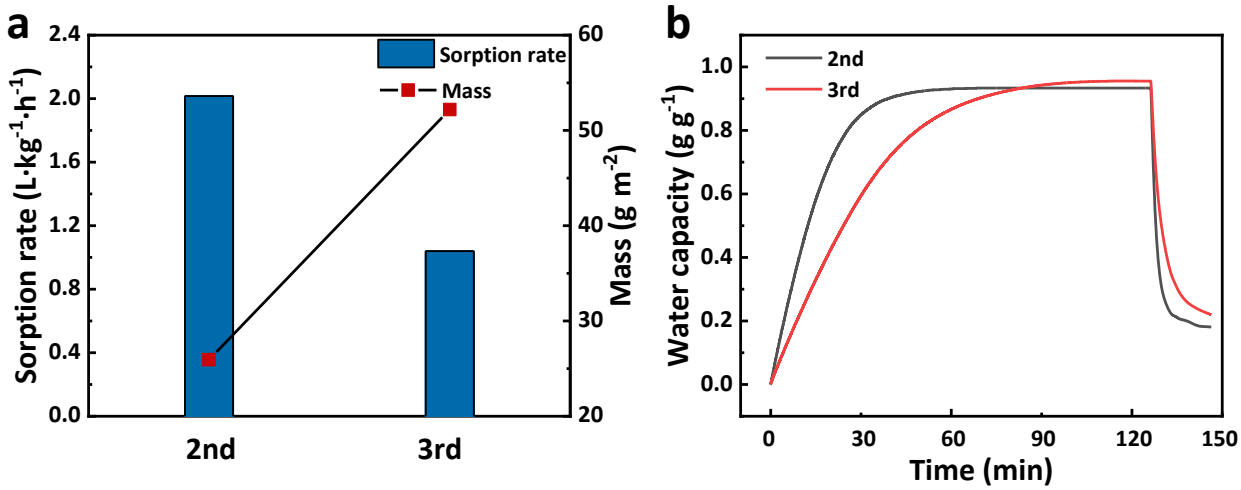

Figure S10. AWH performance of HPHMs with different dip coating-drying cycles. (**a**) sorption rate, mass, (**b**) dynamic sorption, and desorption curves of HPHMs after 2 and 3 times of dip coating-drying cycles on the same adhering area (6.5 cm × 6.5 cm).

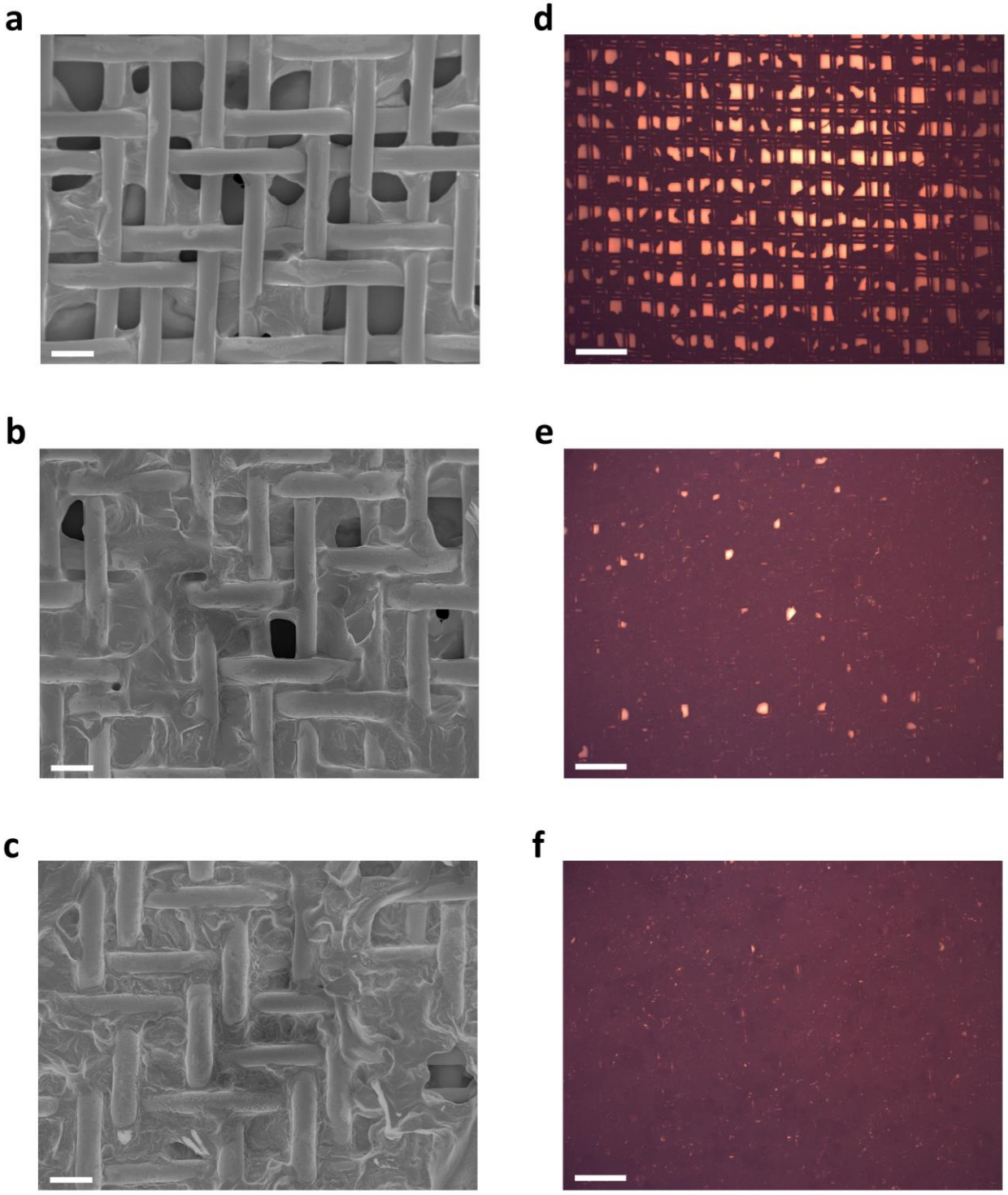

Figure S11. SEM and optical microscope images of HPHMs with different dip coating-drying cycles. SEM (left, scale bar = 100 μm) and optical microscope images (right, scale bar = 400 μm) of dry HPHMs with (**a, d**) 1, (**b**, **e**) 2, and (**c**, **f**) 3 dip coating-drying cycles.

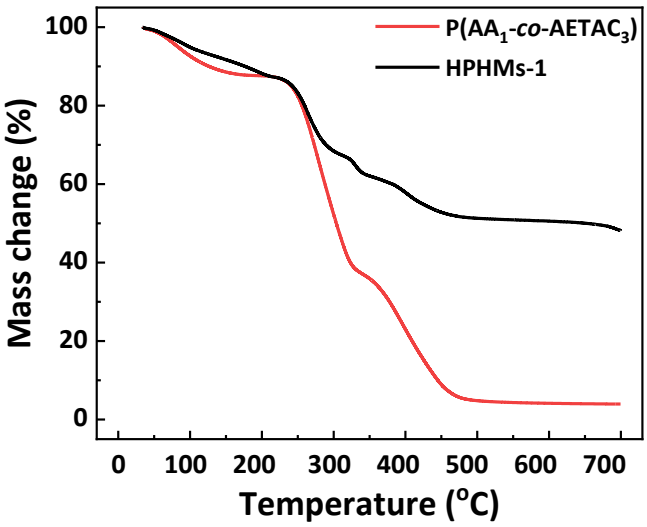

Figure S12. Thermal stability of P(AA_1-*co*-$AETAC_3$) and HPHMs-1. TGA curves of P(AA_1-*co*-$AETAC_3$) (red line) and HPHMs-1 (black line).

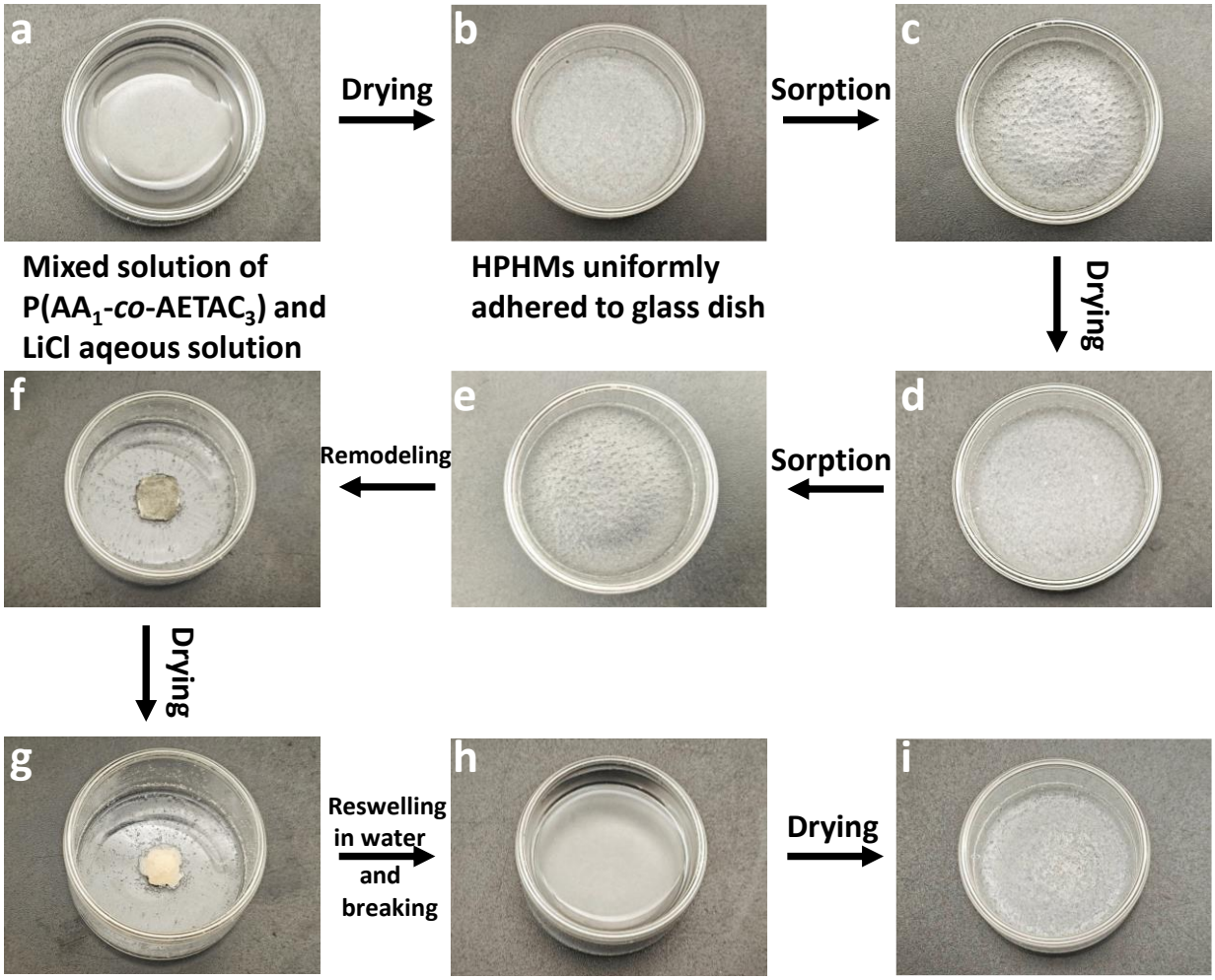

Figure S13. Self-healing of HPHMs. (**a**) The mixed solution of P(AA_1-*co*-$AETAC_3$) and LiCl aqueous solution in a glass evaporating dish was dried, and (**b**) a uniform thin HPHMs hydrogel layer was formed. (**c, d**) The layer was stable after the sorption-desorption process. (**e**) After sorption, HPHMs were remolded into (**f**) sphere and (**g**) dried. (**h**) The sphere was reswelled in DI water and broken by a homogenizer, and (**i**) reformed a uniform thin HPHMs hydrogel layer after drying.

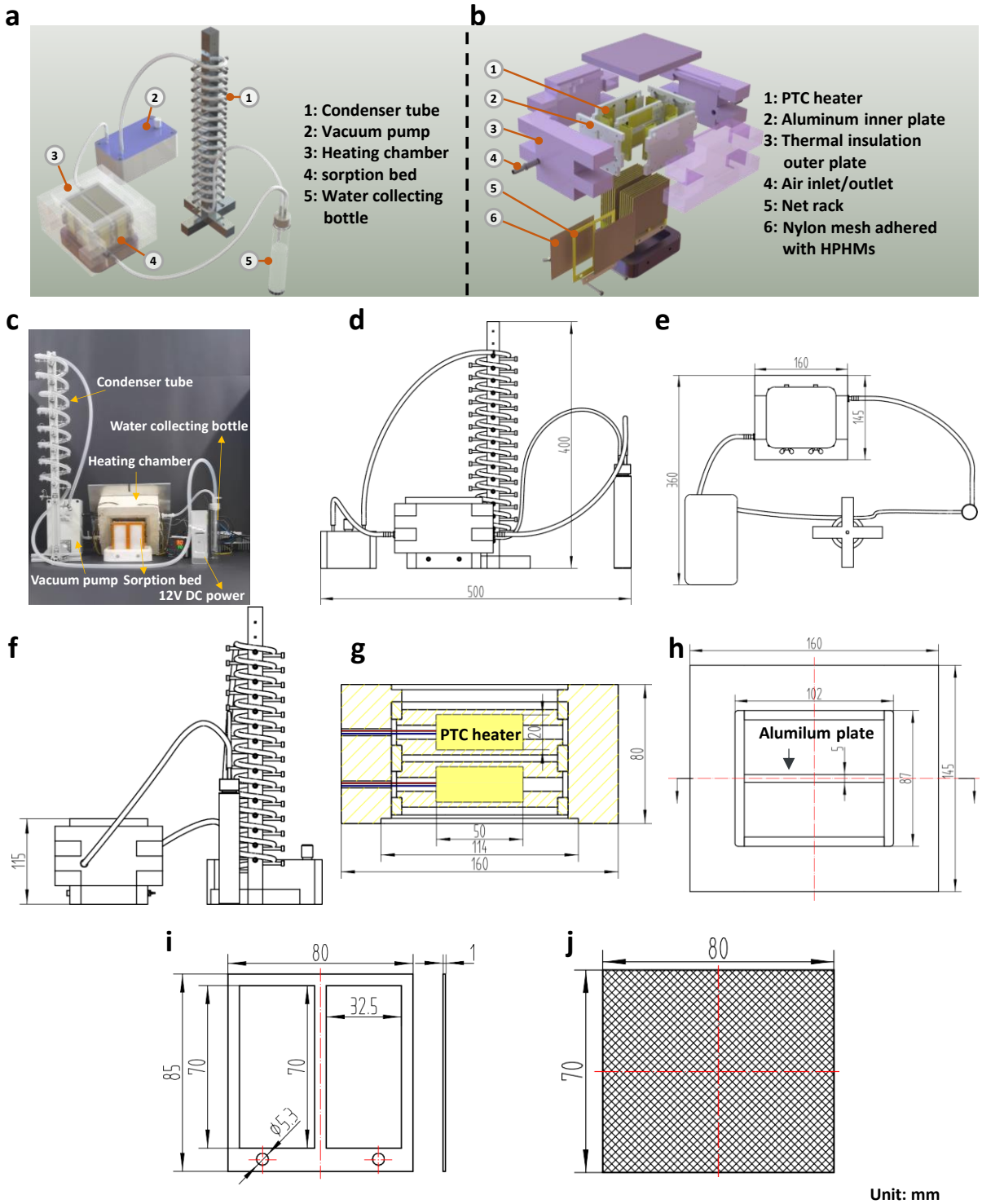

Figure S14. Design of the SAWH test device. Schematic diagram of the structure of (**a**) the SAWH device and (**b**) the heating chamber; (**c**) photo of the AWH device; (**d, f**) side and (**e**) bottom view of the SAWH device; (**g**) cross-section view of the heating chamber; (**h**) bottom view of the heating chamber. Size of (**i**) phenol formaldehyde plastic rack and (**j**) nylon mesh.

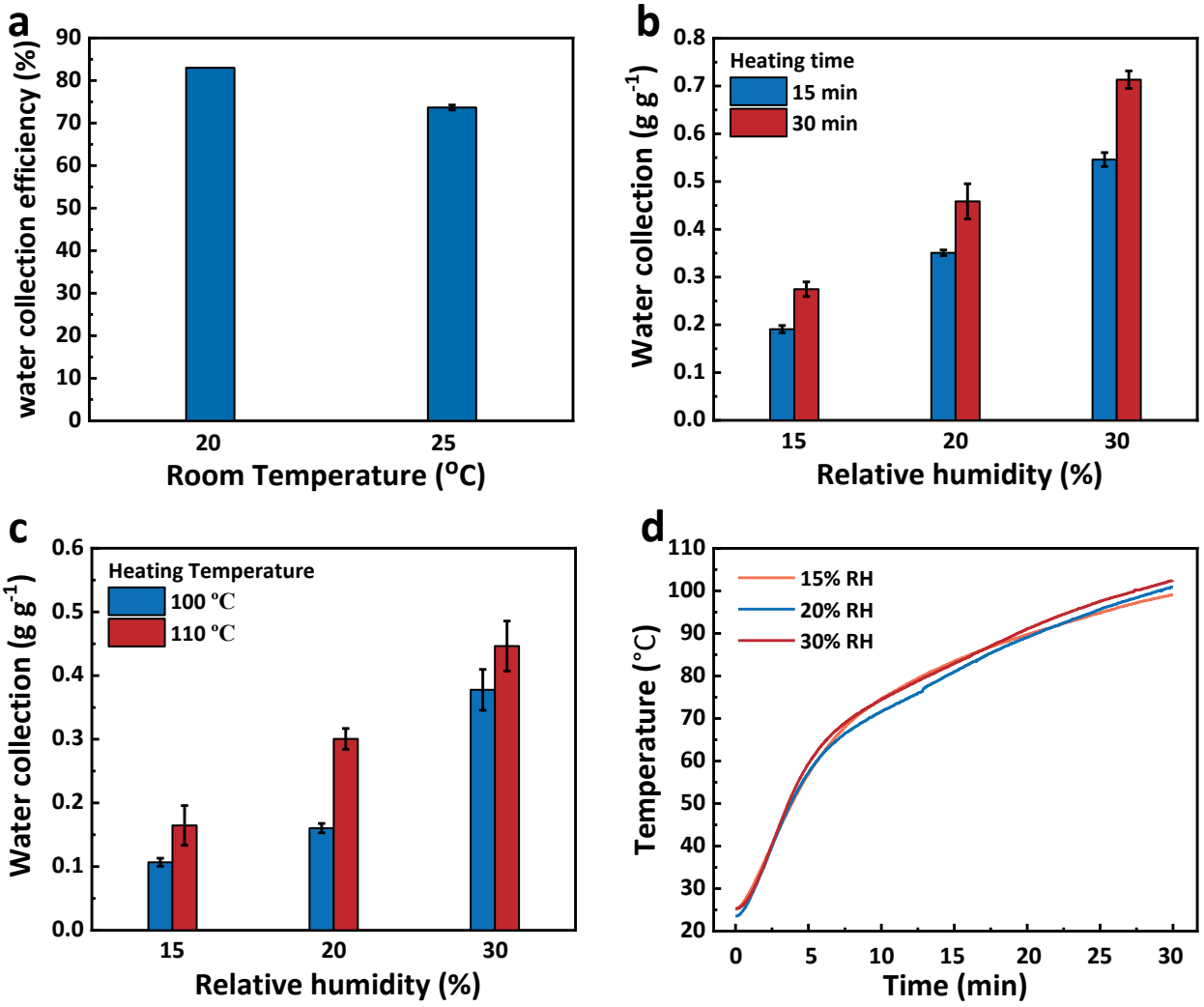

Figure S15. Water collection performance of the SAWH test device. (**a**) Water collection efficiency of the SAWH device. (**b**) water collection of HPHMs-1 at heating plate temperature of 120 °C. (**c**) water collection of HPHMs-1 when the desorption time was 20 min. (**d**) temperature of nylon mesh during water collection.

Figure S16. Water collection of HPHMs-1 in a practical arid environment.

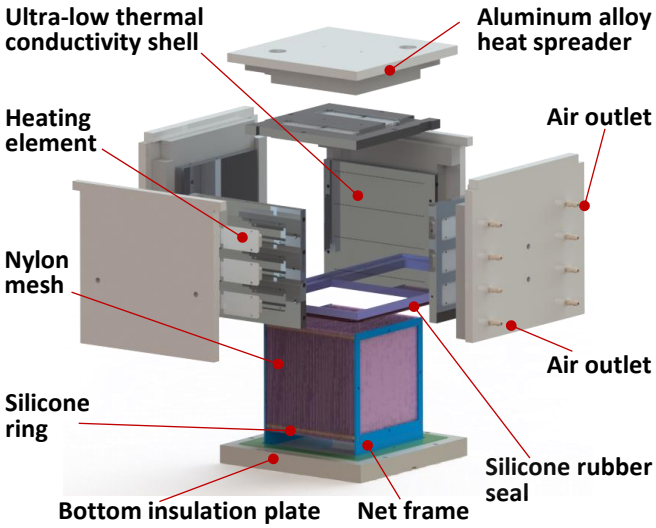

Figure S17. 3D render of the heating module and sorption bed module.

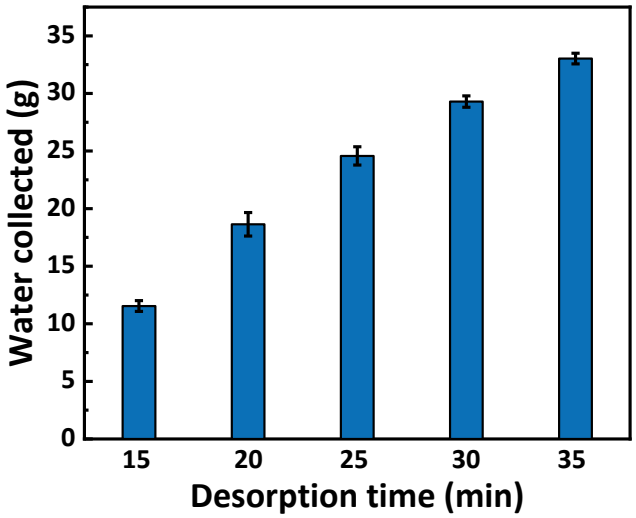

Figure S18. Water collection of HPHMs at different desorption times (25 ℃, 50% RH).

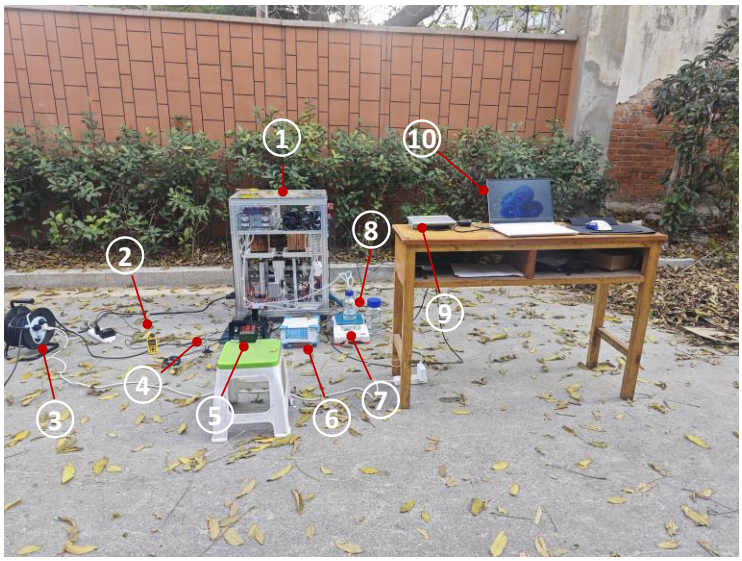

Figure S19. Experimental setup of outdoor water collection. ① automated SAWH device; ② Weather meter; ③ Power supply; ④ Temperature and humidity sensor; ⑤ Digital camera; ⑥ Power meter; ⑦ Electronic balance; ⑧ Water collecting bottle; ⑨ Control panel of automated SAWH device; ⑩ Laptop.

Supplementary Tables

Table S1. Comparison of water collection performance of HPHMs with state-of-the-art SAWH systems.

Ref.	Daily Water collection (g kg^{-1} day^{-1})	Relative humidity and ambient temperature	Absolute water collection (g)	Mass of sorbents (g)	Sorbent type	Heating methods	SAWH system type
This work (test device)	*20180*	18.7-27% RH, 18.3-30.2 ℃	*44.60*	*2.21*	HPHMs	Electric	24 h continuous systems
This work (automated device)	*10500*	45-85.9% RH, 9-20 ℃	*1162*	*110*	HPHMs	Electric	24 h continuous systems
11	2800	20% RH, 25 ℃	8.97	1.79	MOF-801	Solar	Intermittent
49	175	desert	105	600	MOF-303	Solar	Intermittent
46	250	20-40% RH	0.75	3	MOF-801	Solar	Intermittent
33	1310	32% RH, 27 ℃	758	579	MOF-303	Electric	24 h continuous systems
45	840	60% RH, 22 ℃	1.25	1.48	HCS-LiCl	solar	Daytime continuous systems
26	2120	-	46.3	21.8	LiCl@rGO–SA	Solar	Daytime continuous systems
48	110	68% RH, 20 ℃	60	520	AQSOA Z01 (ZEOLITE)	solar	Intermittent
34	3500	17-32% RH, 25 ℃	1400	400	MOF-801	Electric	24 h continuous systems
31	1090	65% RH, 15 ℃	311.69	285.59	Li-SHC	Electric	Intermittent
47	220	35% RH, 20 ℃	7.35	35	MOF-303	solar	Intermittent
30	2,820	60% RH	273	96.8	BHNC	Solar	Intermittent
27	2410	65% RH, 22 ℃	37.09	15.39	PAMPS-CNT-LiCl	Solar + Electric	24 h continuous systems
22	405	55-60% RH, 24-27 ℃	60.8	150	HIPG	Solar	Daytime continuous systems
28	8960	50-90% RH, 22-32 ℃	18	2	CAL gel	Solar	Daytime continuous systems

Table S2. FP parameters of P(AA_x-*co*-$AETAC_y$).

AA: AETAC (molar ratio)	Abbreviation	Frontal temperature (°C)	Frontal velocity (cm min^{-1})
1:0	P(AA_1-*co*-$AETAC_0$)	N/A[1]	N/A[1]
3:1	P(AA_3-*co*-$AETAC_1$)	166.4	12.6
5:3	P(AA_5-*co*-$AETAC_3$)	152.4	15.4
1:1	P(AA_1-*co*-$AETAC_1$)	152.7	17.2
1:3	P(AA_1-*co*-$AETAC_3$)	144.4	11.2
0:1	P(AA_0-*co*-$AETAC_1$)	142.5	6.0

1. Without AETAC, pure AA cannot frontally polymerize. All data are the mean value of three independent experiments.

Table S3. Comparison of AWH performance of HPHMs with state-of-the-art LiCl-based sorbents.

Ref.	Water capacity (g g^{-1}) 30% RH	80% saturation time (min)	Sorption rate (L $kg^{-1}h^{-1}$) (80% saturation)	Desorption time (min) (release 80% captured water)	Desorption rate (L kg^{-1} h^{-1})	Theoretical cycle number (24 h)	Theoretical water collection (L kg^{-1}) (24 h)
This work	0.91	*13.5*	*3.22*	10 min at 70 ℃	*4.36*	*61*	*33.3*
45	0.7	180	0.18	-	-	-	-
26	1.52	100	0.72	85 min at 90 ℃	0.85	7	6.38
25	0.8	20	1.92	16.5 min at 60 ℃	2.32	39	18.72
23	0.96	36	1.28	15.5 min at 60 ℃	2.97	27	15.55
41	0.62	60	0.49	20 min at 80 ℃	1.48	18	6.69
24	1.5	70	1.02	25 min at 70 ℃	2.88	15	13.5
31	1.79	80	1.07	-	-	-	-
52	0.5	425	0.056	-	-	-	-
21	0.77	22	1.68	7 min at 1 sun	5.28	49	22.6
27	1	175	0.27	55 min at 90 ℃	0.87	6	3.6
30	1.36	60	1.08	16 min at 90 ℃	4.08	18	14.68
55	1.66	60	1.32	18.5 min at 1 sun	3.44	18	17.92
53	1.08	90	0.57	85 min at 1 sun	0.64	8	5.18
28	0.79	37	1.02	-	-	-	-

22	1.01	20	2.4	20 min at 1 sun	2.42	36	21.81
39	1.81	69	1.25	51 min at 1 sun	1.70	12	13.03
50	0.9	29	1.48	-	-	-	-
51	0.75	71.5	0.50	-	-	-	-
56	1.64	195	0.50	20 min at 90 ℃	3.93	6	5.90
38	1.2	155	0.37	92 min at 80 ℃	0.62	5	3.6
54	1.32	60	1.05	12.5 min at 60 ℃	5.06	19	15.04

306

Table S4. Concentrations of primary metal elements in collected water measured by Inductively Coupled Plasma (ICP) analysis.

	Concentration (mg L^{-1})	Guideline from WHO (mg L^{-1})
Li	0.0161	N/A
Na	1.27	50
Ca	0.0354	200
Zn	0.00213	0.3
Cu	0.00298	2
Pb	0.00628	3
Fe	0.000106	0.01

Table S5. Concentrations of possible ions in collected water measured by Ion Chromatography.

	Concentration (mg L^{-1})	Guideline from WHO (mg L^{-1})
F^-	0.8577	1.5
Cl^-	6.6088	250
Br^-	N/A	N/A
NO_3^-	0.522	50
SO_4^-	2.292	500

Supplementary Videos

Video S1. Frontal polymerization of P(AA_1-*co*-$AETAC_3$) in tube recorded by digital camera

Video S2. Frontal polymerization of P(AA_1-*co*-$AETAC_3$) in tube recorded by thermal infrared camera

Video S3. 1 kg P(AA_1-*co*-$AETAC_3$) fabricated by frontal polymerization recorded by digital camera

Video S4. Thermal infrared image of 1 kilogram P(AA_1-*co*-$AETAC_3$) fabricated by frontal polymerization

Video S5. Water collection of the SAWH device

Video S6. Exchange the sorption beds of the automated SAWH device

Video S7. 24-hour continuous water collection of HPHMs by the automated SAWH device

References

1. Water Science School, The distribution of water on, in, and above the Earth. *USGS*. https://www.usgs.gov/media/images/distribution-water-and-above-earth (2019).
2. M. M. Mekonnen, A. Y. Hoekstra, Four billion people facing severe water scarcity. *Sci. Adv*. **2**, e1500323 (2016).
3. He, C., Liu, Z., Wu, J. et al. Future global urban water scarcity and potential solutions. *Nat Commun.* **12**, 4667 (2021).
4. Y. Tu, R. Wang, Y. Zhang, J. Wang, Progress and Expectation of Atmospheric Water Harvesting. *Joule*. **2**, 1452-1475 (2018).
5. M. Wang, E. Liu, T. Jin, S.-u. Zafar, X. Mei, M.-L. Fauconnier, C. De Clerck, Towards a better understanding of atmospheric water harvesting (AWH) technology. *Water Res*. **250**, 121052 (2024).
6. C. Lei, W. Guan, Y. Zhao, G. Yu, Chemistries and materials for atmospheric water harvesting. *Chem. Soc. Rev*. **53**, 7328-7362 (2024).
7. H. Shan, P. Poredoš, Z. Chen, X. Yang, Z. Ye, Z. Hu, R. Wang, S. C. Tan, Hygroscopic salt-embedded composite materials for sorption-based atmospheric water harvesting. *Nat. Rev. Mater*. **9**, 699-721 (2024).
8. Y. Zhong, L. A. Zhang, X. Y. Li, B. El Fil, C. D. Diaz-Marin, A. C. Li, X. Y. Liu, A. Lapotin, E. N. Wang, Bridging materials innovations to sorption-based atmospheric water harvesting devices. *Nat. Rev. Mater*. **9**, 681-698 (2024).
9. R. Li, P. Wang, Sorbents, processes and applications beyond water production in sorption-based atmospheric water harvesting. *Nat. Water*. **1**, 573-586 (2023).
10. W. Shi, W. Guan, C. Lei, G. Yu, Sorbents for Atmospheric Water Harvesting: From Design Principles to Applications. *Angew. Chem., Int. Ed*. **61**, e202211267 (2022).
11. H. Kim, S. Yang, S. R. Rao, S. Narayanan, E. A. Kapustin, H. Furukawa, A. S. Umans, O. M. Yaghi, E. N. Wang, Water harvesting from air with metal-organic frameworks powered by natural sunlight. *Science*. **356**, 430-432 (2017).
12. N. Hanikel, M. S. Prevot,O. M. Yaghi, MOF water harvesters. *Nat. Nanotechnol*. **15**, 348-355 (2020).
13. Y. Song, N. Xu, G. Liu, H. Qi, W. Zhao, B. Zhu, L. Zhou, J. Zhu, High-yield solar-driven atmospheric water harvesting of metal-organic-framework-derived nanoporous carbon with fast-diffusion water channels. *Nat. Nanotechnol*. **17**, 857-863 (2022).
14. H. L. Nguyen, N. Hanikel, S. J. Lyle, C. Zhu, D. M. Proserpio, O. M. Yaghi, A Porous Covalent Organic Framework with Voided Square Grid Topology for Atmospheric Water Harvesting. *J. Am. Chem. Soc*. **142**, 2218-2221 (2020).
15. H. L. Nguyen, Covalent Organic Frameworks for Atmospheric Water Harvesting. *Adv. Mater*. **35**, 2300018 (2023).
16. Z. Shi, Y. Guo, X. Zou, J. Zhang, Z. Chen, M. Shan, Z. Zhang, S. Guo, F. Yan, Low Evaporation Enthalpy Ionic Covalent Organic Frameworks for Efficient Atmospheric Water Harvesting at Low Humidity. *Angew. Chem., Int. Ed*. **64**, e202420619 (2025).

17. F. Zhao, X. Zhou, Y. Liu, Y. Shi, Y. Dai, G. Yu, Super Moisture-Absorbent Gels for All-Weather Atmospheric Water Harvesting. *Adv. Mater*. **31**, 1806446 (2019).

18. H. Yao, P. Zhang, Y. Huang, H. Cheng, C. Li, L. Qu, Highly Efficient Clean Water Production from Contaminated Air with a Wide Humidity Range. *Adv. Mater*. **32**, 1905875 (2020).

19. M. Wu, R. Li, Y. Shi, M. Altunkaya, S. Aleid, C. Zhang, W. Wang, P. Wang, Metal- and halide-free, solid-state polymeric water vapor sorbents for efficient water-sorption-driven cooling and atmospheric water harvesting. *Mater. Horiz*. **8**, 1518-1527 (2021).

20. J. Xu, T. Li, J. Chao, S. Wu, T. Yan, W. Li, B. Cao, R. Wang, Efficient Solar-Driven Water Harvesting from Arid Air with Metal-Organic Frameworks Modified by Hygroscopic Salt. *Angew. Chem., Int. Ed*. **59**, 5202-5210 (2020).

21. M. Xia, D. Cai, J. Feng, P. Zhao, J. Li, R. Lv, G. Li, L. Yan, W. Huang, Y. Li, Z. Sui, M. Li, H. Wu, Y. Shen, J. Xiao, D. Wang, Q. Chen, Biomimetic Hygroscopic Fibrous Membrane with Hierarchically Porous Structure for Rapid Atmospheric Water Harvesting. *Adv. Funct. Mater*. **33**, 2214813 (2023).

22. X. Yang, Z. Chen, C. Xiang, H. Shan, R. Wang, Enhanced continuous atmospheric water harvesting with scalable hygroscopic gel driven by natural sunlight and wind. *Nat. Commun*. **15**, 7678 (2024).

23. Y. Guo, W. Guan, C. Lei, H. Lu, W. Shi, G. Yu, Scalable super hygroscopic polymer films for sustainable moisture harvesting in arid environments. *Nat. Commun*. **13**, 2761 (2022).

24. H. Lu, W. Shi, J. H. Zhang, A. C. Chen, W. Guan, C. Lei, J. R. Greer, S. V. Boriskina, G. Yu, Tailoring the Desorption Behavior of Hygroscopic Gels for Atmospheric Water Harvesting in Arid Climates. *Adv. Mater*. **34**, 2205344 (2022).

25. W. Guan, C. Lei, Y. Guo, W. Shi, G. Yu, Hygroscopic-Microgels-Enabled Rapid Water Extraction from Arid Air. *Adv. Mater*. **36**, 2207786 (2022).

26. J. Xu, T. Li, T. Yan, S. Wu, M. Wu, J. Chao, X. Huo, P. Wang, R. Wang, Ultrahigh solar-driven atmospheric water production enabled by scalable rapid-cycling water harvester with vertically aligned nanocomposite sorbent. *Energy Environ. Sci*. **14**, 5979-5994 (2021).

27. H. Shan, P. Poredos, Z. Y. Ye, H. Qu, Y. X. Zhang, M. J. Zhou, R. Z. Wang, S. C. Tan, All-Day Multicyclic Atmospheric Water Harvesting Enabled by Polyelectrolyte Hydrogel with Hybrid Desorption Mode. *Adv. Mater*. **35**, 2302038 (2023).

28. H. Zhou, L. Yan, D. Tang, T. Xu, L. Dai, C. Li, W. Chen, C. Si, Solar‐Driven Drum‐Type Atmospheric Water Harvester Based on Bio‐Based Gels with Fast Adsorption/Desorption Kinetics. *Adv. Mater*. **36**, 2403876 (2024).

29. C. Liu, X.-Y. Yan, S. Li, H. Zhang, B. Deng, N. X. Fang, Y. Habibi, S.-C. Chen, X. Zhao, A metre-scale vertical origami hydrogel panel for atmospheric water harvesting in Death Valley. *Nat. Water*. **3**, 714-722 (2025).

30. T. Li, T. Yan, P. Wang, J. Xu, X. Huo, Z. Bai, W. Shi, G. Yu, R. Wang, Scalable and efficient solar-driven atmospheric water harvesting enabled by bidirectionally aligned and hierarchically structured nanocomposites. *Nat. Water*. **1**, 971-981 (2023).

31. H. Shan, C. Li, Z. Chen, W. Ying, P. Poredoš, Z. Ye, Q. Pan, J. Wang, R. Wang, Exceptional water production yield enabled by batch-processed portable water harvester in semi-arid climate. *Nat. Commun*. **13**, 5406 (2022).

32. Z. Bai, P. Wang, J. Xu, R. Wang, T. Li, Progress and perspectives of sorption-based atmospheric water harvesting for sustainable water generation: Materials, devices, and systems. *Sci. Bull*. **69**, 671-687 (2024).

33. N. Hanikel, M. S. Prévot, F. Fathieh, E. A. Kapustin, H. Lyu, H. Wang, N. J. Diercks, T. G. Glover, O. M. Yaghi, Rapid Cycling and Exceptional Yield in a Metal-Organic Framework Water Harvester. *ACS Cent. Sci*. **5**, 1699-1706 (2019).

34. H. A. Almassad, R. I. Abaza, L. Siwwan, B. Al-Maythalony, K. E. Cordova, Environmentally adaptive MOF-based device enables continuous self-optimizing atmospheric water harvesting. *Nat. Commun*. **13**, 4873 (2022).

35. G. Graeber, C. D. Diaz-Marin, L. C. Gaugler, Y. Zhong, B. El Fil, X. Liu, E. N. Wang, Extreme Water Uptake of Hygroscopic Hydrogels through Maximized Swelling-Induced Salt Loading. *Adv. Mater*. **36**, 2211783 (2023).

36. H. Zou, X. Yang, J. Zhu, F. Wang, Z. Zeng, C. Xiang, D. Huang, J. Li, R. Wang, Solar-driven scalable hygroscopic gel for recycling water from passive plant transpiration and soil evaporation. *Nat. Water*. **2**, 663-673 (2024).

37. X. Zhang, H. Qu, X. Li, L. Zhang, Y. Zhang, J. Yang, M. Zhou, L. Suresh, S. Liu, S. C. Tan, Autonomous Atmospheric Water Harvesting over a Wide RH Range Enabled by Super Hygroscopic Composite Aerogels. *Adv. Mater*. **36**, 2310219 (2024).

38. X. Du, Z. Xie, H. Zhang, S. Jiang, X. Su, J. Fan, Robust Mix‐Charged Polyzwitterionic Hydrogels for Ultra‐Efficient Atmospheric Water Harvesting and Evaporative Cooling. *Adv. Mater*. **37**, 2505279 (2025).

39. H. Guo, Q. Luo, D. Liu, X. Li, C. Zhang, X. He, C. Miao, X. Zhang, X. Qin, Super Moisture‐Sorbent Sponge for Sustainable Atmospheric Water Harvesting and Power Generation. *Adv. Mater*. **36**, 2414285 (2024).

40. B. A. Suslick, J. Hemmer, B. R. Groce, K. J. Stawiasz, P. H. Geubelle, G. Malucelli, A. Mariani, J. S. Moore, J. A. Pojman, N. R. Sottos, Frontal Polymerizations: From Chemical Perspectives to Macroscopic Properties and Applications. *Chem. Rev*. **123**, 3237-3298 (2023).

41. C. Lei, Y. Guo, W. Guan, H. Lu, W. Shi, G. Yu, Polyzwitterionic Hydrogels for Efficient Atmospheric Water Harvesting. *Angew. Chem., Int. Ed*. **61**, e202200271 (2022).

42. D. Li, Z. Xu, Ji. X, Ji, L. Liu, G, Gai, J. Yang, J. Wang, Deep insight into ionic transport in polyampholyte gel electrolytes towards high performance solid supercapacitors. *J. Mater. Chem. A*. **7**, 16414-16424 (2019).

43. X. Zhang, J. Hansing, Roland R. Netz, Jason E. DeRouchey, Particle Transport through Hydrogels Is Charge Asymmetric. *Biophys. J.* **108**, 530-539 (2015).

44. J. Hansing, J. R. Duke, E. B. Fryman, J. E. DeRouchey, R. R. Netz, Particle Diffusion in Polymeric Hydrogels with Mixed Attractive and Repulsive Interactions. *Nano Lett.* **18**, 5248-5256 (2018).

45. R. Li, Y. Shi, M. Wu, S. Hong, P. Wang, Improving atmospheric water production yield: Enabling multiple water harvesting cycles with nano sorbent. *Nano Energy*. **67**, 104255 (2020).

46. H. Kim, S. R. Rao, E. A. Kapustin, L. Zhao, S. Yang, O. M. Yaghi, E. N. Wang, Adsorption-based atmospheric water harvesting device for arid climates. *Nat. Commun*. **9**, 1191 (2018).

47. W. Song, Z. Zheng, A. H. Alawadhi, O. M. Yaghi, MOF water harvester produces water from Death Valley desert air in ambient sunlight. *Nat. Water*. **1**, 626-634 (2023).

48. A. LaPotin, Y. Zhong, L. Zhang, L. Zhao, A. Leroy, H. Kim, S. R. Rao, E. N. Wang, Dual-Stage Atmospheric Water Harvesting Device for Scalable Solar-Driven Water Production. *Joule*. **5**, 166-182 (2021).

49. F. Fathieh, M. J. Kalmutzki, E. A. Kapustin, P. J. Waller, J. J. Yang, O. M. Yaghi, Practical water production from desert air. *Sci. Adv*. **4**, eaat3198 (2018).

50. J. Wang, W. Ying, B. Lin, C. Li, C. Deng, H. Zhang, S. Wang, R. Wang, Tillandsia-Inspired Ultra-Efficient Thermo-Responsive Hygroscopic Nanofibers for Solar-Driven Atmospheric Water Harvesting. *Adv. Mater*. **37**, 2408977 (2024).

51. Y. Lee, S. H. Nah, K.-Y. Wang, Y. Chi, J. B. Kim, Z. Zhang, S. Yang, Highly Scalable, Raspberry-Like Microbeads with Nano-/Micro-Confined Hybrid Hydrogel Desiccants for Rapid Atmospheric Water Harvesting. *Adv. Funct. Mater*. **35**, 2506725 (2025).

52. S. Aleid, M. Wu, R. Li, W. Wang, C. Zhang, L. Zhang, P. Wang, Salting-in Effect of Zwitterionic Polymer Hydrogel Facilitates Atmospheric Water Harvesting. *ACS Mater. Lett*. **4**, 511-520 (2022).

53. J. Sun, F. Ni, J. Gu, M. Si, D. Liu, C. Zhang, X. Shui, P. Xiao, T. Chen, Entangled Mesh Hydrogels with Macroporous Topologies via Cryogelation for Rapid Atmospheric Water Harvesting. *Adv. Mater*. **36**, 2314175 (2024).

54. W. Guan, Y. Zhao, C. Lei, Y. Wang, K. Wu, G. Yu, Molecularly Functionalized Biomass Hydrogels for Sustainable Atmospheric Water Harvesting. *Adv. Mater*. **37**, 2420319 (2025).

55. Z. Yu, S. Li, J. Zhang, C. Tang, Z. Qin, X. Liu, Z. Zhou, Y. Lai, S. Fu, Phospholipid Bilayer Inspired Sandwich Structural Nanofibrous Membrane for Atmospheric Water Harvesting and Selective Release. *Nano Lett*. **24**, 2629-2636 (2024).

56. B. Lin, W. Ying, C. Li, J. Liu, L. Zhou, H. Zhang, R. Wang, J. Wang, Biomass-Derived Hydro-Sponge for Ultra-Efficient Atmospheric Water Harvesting. *Adv. Funct. Mater*. **35,** 2500679 (2025).